Quantitativeness of phase-field simulations for directional solidification of faceted silicon monograins in thin samples

Terkia Braik, Ahmed Kaci Boukellal, Jean-Marc Debierre

Quantitativeness of phase-field simulations for directional solidification of faceted silicon monograins in thin samples.

Terkia Braik[1], Ahmed Kaci Boukellal[2*], and Jean-Marc Debierre[1†]
[1] *Aix-Marseille Université, CNRS, Université de Toulon, IM2NP UMR 7334, 13397 Marseille, France*
[2] *IMDEA Materials Institute, Getafe, Madrid, Spain*

(Dated: October 14, 2022)

We report the results of a two-dimensional reference model for the formation of facets on the left and the right side of a silicon monograin that is solidified by pulling a thin sample in a constant temperature gradient. Anisotropy functions of both the surface energy and the kinetic attachment coefficient are adapted from a recent model for free growth of silicon micrometer size grains [Boukellal et al., J. Cryst. Growth **522**, 37 (2019)]. More precise estimates of the physical parameters entering these functions are obtained by reanalyzing available experimental results. We show that the reference model leads to a differential equation for the shape of the solid-liquid interface. The numerical solutions of this equation give a reference law $\Lambda(V_f)$ relating the facet length Λ to the facet normal velocity V_f. In parallel, phase-field simulations of the reference model are performed for two growth orientations, [001] and [011]. Facet lengths Λ obtained from simulations at different facet velocities are first extrapolated to the limit of vanishing interface width. This extrapolation is made possible by constructing a master curve common to the whole range of V_f values considered. The extrapolated Λ values are then compared with the ones predicted by the $\Lambda(V_f)$ reference law. Both sets give comparable values, with an accuracy of a few percent, which confirms that the phase-field model can give quantitative results for faceted solidification of silicon.

PACS numbers: 81.10.Aj, 68.70.+w, 81.30.Fb
Keywords:

I. INTRODUCTION

Over the last decades, several generations of solar cells have been developed to speed up the fossil energy replacement [1]. Nowadays, silicon-based solar cells are still widely used [2, 3], notably because of the remarkable electronic properties of silicon [4]. However, controlling sufficiently the solidification of silicon to improve the photovoltaics properties at reasonable cost remains an important economical issue [3]. It is indeed well reckoned that the structural and chemical defects of solidified silicon have a direct impact on solar cell performances [3, 5–7].

Crystalline silicon exhibits facets at the solid-liquid interface, as is predicted by Jackson Criterion [8], and is consistently shown by experiments [9, 10] and reproduced by atomic-scale simulations [9, 11–13]. In particular, it is well-known that silicon solidification shapes develop large {111} facets because, as compared to the other orientations, kinetic attachment effects considerably slow down the growth of these compact atomic planes [14–17]. In order to include faceting in growth models, two main points of view have been advanced in the literature. A first one is to consider fully (or almost fully) faceted shapes. In this case fundamental questions arise at the corner points where several facets meet. This point of view has given rise to a number of fundamental studies [18–20] and to elegant solutions concerning the singularities at corner points [21, 22].

The second point of view is more adapted to partially faceted interfaces like the ones usually observed for a solid silicon germ in contact with its melt [10, 17]. In this case, facets only appear for a discrete set of orientations, namely the eight ⟨111⟩ directions in the present case, and these facets are separated by large rough portions of the interface. As shown in [23], it is necessary that both anisotropy functions associated with the surface energy γ and the kinetic attachment coefficient β present singularities in the ⟨111⟩ directions, in order to account for the large facets observed in [10, 17]. This is the point of view that we will adopt here, based on the aforementioned experimental, numerical, and analytical results, as well as on our previous phase-field studies of equiaxed faceted solidification in two [24] and in three dimensions [23].

About two decades ago, the use of phase-field solidification simulations was considerably boosted by the introduction of the thin interface formalism that was proved to give quantitative results for both pure elements [25] and binary alloys [26, 27]. Most of the phase-field studies were carried out for materials exhibiting a rough solid-liquid interface. In such situations, the kinetic attachment effects are negligible and the anisotropy functions of surface energy consist essentially in linear combinations of the spherical harmonics taking into account the symmetry of the material. However, when it comes to perform quantitative simulations of solidification of materials ex-

*Present address : Institut Jean Lamour, Nancy, France
†Corresponding author: jean-marc.debierre@im2np.fr

hibiting a faceted solid-liquid interface like silicon, kinetic attachment effects should be taken into account and obtaining reasonable expressions for the anisotropy functions associated with γ and β becomes a serious limiting step. Different anisotropy functions have been proposed in the literature but they generally depend on adjustable numerical parameters that have no direct physical counterparts [28–30] so quantitative comparison with experiment is difficult. A review of such functions with a short description of their qualities and drawbacks was recently published [31].

In a recent study [23], we proposed anisotropy functions that were based on experimental results and symmetry considerations. These anisotropies were used to simulate Si solidification in conditions close to reference experiments [10]. The good agreement found between numerics and experiments validated to a large extent the proposed anisotropy functions. Here, we recalibrate these functions by reanalyzing available experimental data and we use them to perform simulations of directional solidification of pure Si. The goal of the present paper is to show that one can obtain a quantitative phase-field model for this problem.

The paper is organized as follows. In section II, a two-dimensional (2D) reference model is defined to describe the steady-state solidification of a Si monograin. The solid-liquid interface is composed of a central rough segment matching tangentially two facets that contact the domain side boundaries. The appropriate interface equation is discussed for the rough and the faceted segments. In addition, the analytical form of the anisotropy functions are given for γ and β. Section III presents the bases of our phase-field model and the phase field evolution equation is given. Based on available experimental data, anisotropy parameters are adjusted. Implementation of the phase-field code is then presented, in particular the criterion used to measure facet lengths and its implications on the choice of the kinetic attachment amplitude in the code. An extended list of the physical and numerical simulation parameters is also provided. The phase-field results obtained for the steady-state growth shapes are presented and analyzed in section IV. There, the emphasis is put on convergence of the simulation results with decreasing interface width. It is shown that converged values Λ_0 of the facet length can be obtained with the help of a master curve that takes into account the influence of the normal facet velocity V_f on phase field diffusion across the interface region along a facet. The reference model is then treated analytically in section V, where a differential equation is obtained for the rough segment of the interface. Solving this equation by a finite-difference algorithm gives an exact correspondance between the facet length Λ and V_f. Direct comparison with the phase-field converged values $\Lambda_0(V_f)$ shows excellent agreement, within a few percent. Finally, our main conclusions are summarized in section VI, and a few prospective points are evoked.

II. REFERENCE 2D MODEL

We focus on the case of a Si monograin that is solidified by pulling a thin sample at a velocity V toward the cold region of a furnace. A constant temperature gradient $\vec{G}$ is imposed by the furnace, and both $\vec{G}$ and the stationary growth velocity $\vec{V}$ are directed along the vertical z axis as shown in Fig. 1a. The temperature gradient is assumed positive, so a planar interface must remain stable independently of the pulling velocity. In the experiments, facets are nevertheless observed on both sides of the sample as a result of the Herring equation [32] that governs the solid-liquid-vacuum triple junctions (Fig. 1b).

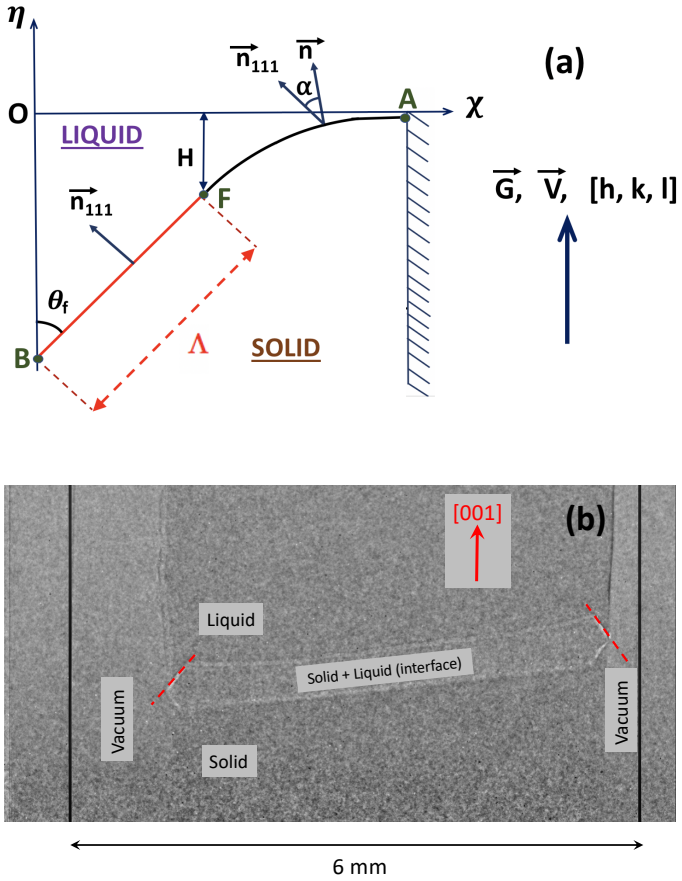

FIG. 1: (a) Schematic representation of the 2D model discussed in the text. The solid-liquid interface is represented by a straight line of length Λ (faceted segment BF) that matches tangentially a curve (rough segment FA) at point F. The frame of reference is linked to the $T = T_m$ isotherm located at $z = z_m$ ($\eta = 0$). A vertical mirror symmetry is assumed at the solid apex (point A). (b) Experimental *in situ* X-ray image showing the slanted interfacial region (central lighter strip) in a thin silicon ingot (courtesy of N. Mangelinck-Noël and G. Reinhart). The crucible width is about 6 mm. Silicon fills completely the crucible in the direction perpendicular to the figure (300 μm thick) but it does not fill the complete crucible width, so vacuum regions remain on the sides. Dotted lines parallel to the side facets are added to guide the eye.

As shown in Fig. 2, we independently consider two simple crystal orientations for which a first crystal axis, [001] (respectively [011]), lies along the z axis and a second crystal axis, [110] (respectively [01$\bar{1}$]), lies along the y axis perpendicular to the sample. Our reference model is restricted to the plane xz, that is we consider 2D systems for both orientations. As illustrated in Fig. 2, this model is only an approximation of a real 3D system. The approximation is definitely better for the [011] crystal orientation for which a straight edge common to two {111} facets parallels the y axis than for the [001] direction for which the apex is common to four adjacent {111} facets, so invariance along y is broken. Although the present 2D model would not perfectly describe a bulk sample, we will still use it for two reasons. First, we will see that it is possible to obtain an analytical equation for the interface in 2D systems, the corresponding equation being not yet completely known for 3D systems. Second, the phase-field simulations we present here are still too demanding (both in time and storage) to be performed in fully 3D domains. In the following, we will nevertheless keep 3D notations for the crystal planes and directions because both the experiments and the phase-field model we refer ourselves to are 3D.

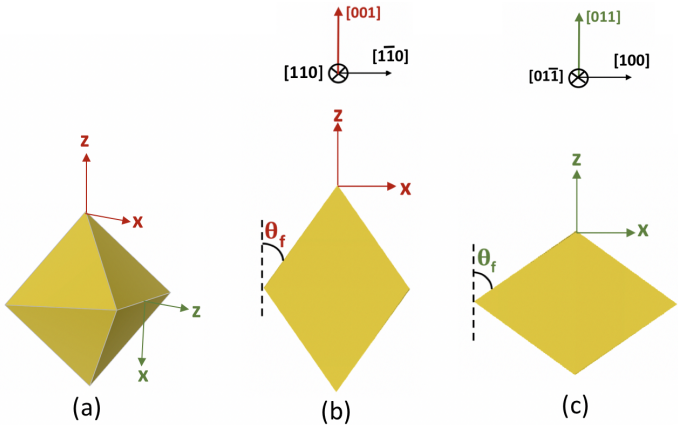

FIG. 2: (a) Octahedron representing the diamond crystal structure. (b) Cross-section in a ⟨200⟩ plane with a {001} crystal axis in the growth direction. (c) Cross-section in a ⟨200⟩ plane with a {011} crystal axis in the growth direction. The actual crystalline directions taken for the numerical domain axes x, y, z are indicated above (b) and (c). The corresponding values of the facet angle θ_f are given in Table I.

A. Interface equations

In the literature on Si solidifying from its pure melt, it has consistently been observed that only {111} facets appear [14–17]. In the present case, the shape adopted by the solid-liquid interface is schematically represented in Fig. 1a. The side facet has a length Λ and it lies precisely at a crystallographic angle θ_f about the z axis. This ideal facet ends at point F, where it matches tangentially the rough part of the interface. In the following, we will consider the case of perfectly symmetric interfaces, so only half of the domain width is represented with a mirror boundary condition on the right side. In this 2D model, crystal anisotropy functions only depend on the conical angle α between the normal to interface and the ⟨111⟩ direction. Due to the presence of {111} facets, a singulariy at $\alpha = 0$ is thus expected for the surface free energy

$$\gamma(\alpha) = \gamma_0 a_s(\alpha), \tag{1}$$

γ_0 being the average surface energy at T_m and $a_s(\alpha)$ the anisotropy function. In the following, we assume that a_s has a cusp at $\alpha = 0$. As described in [23, 24], this cusp causes a discontinuity of the surface stiffness $\gamma_0\left[a_s(\alpha)+d^2a_s(\alpha)/d\alpha^2\right]$ for $\alpha = 0$. In the present model, a similar discontinuity is assumed for the kinetic attachment coefficient.

$$\beta(\alpha) = \beta_{111} b_k(\alpha), \tag{2}$$

β_{111} being the physical value of the kinetic attachment coefficient for the {111} facets. The corresponding anisotropy function $b_k(\alpha) = 0$ when $\alpha \neq 0$ and $b_k(0) = 1$.

Solidification is governed by physical equations that involve the nondimensional temperature field

$$u = \frac{c_p}{l_H}(T - T_m), \tag{3}$$

c_p being the specific heat at constant pressure, l_H the specific latent heat and T_m the silicon melting temperature. We will consider the case of a frozen temperature field $T(z) = T_m + G(z - z_m)$, where z_m is the altitude of the isotherm $T = T_m$. We place ourselves in the reference frame of the temperature isotherm, where z_m is constant in time. At any point along the rough part of the interface, thermodynamic equilibrium is ensured by the Gibbs-Thomson equation,

$$u_i = -\frac{d_T(\alpha)}{R_i}, \tag{4}$$

with R_i the local interface radius of curvature, and

$$d_T(\alpha) = d_0\left[a_s(\alpha) + d^2a_s(\alpha)/d\alpha^2\right], \tag{5}$$

where $d_0 = c_p\gamma_0 T_m/l_H^2$ is the thermal capillary length. For the faceted part of the interface, Gibbs-Thomson equation can no longer be used because u_i varies with z along the facet. Ben Amar and Pomeau (BAP) proposed to use an integral equation instead [33]. This equation reads

$$\Lambda\overline{u} = \int_{s-}^{s+} u_T ds = -d_0[da_s/d\alpha|_{0^+} - da_s/d\alpha|_{0^-}] - \Lambda\beta_{111}V_f, \tag{6}$$

where, s^+ and s^- are the curvilinear coordinates of the facets ends ($\alpha \to 0^+$ and 0^- respectively). According to Fig. 1a, the facet normal velocity V_f is related to the pulling velocity V through

$$V_f = V \sin\theta_f. \tag{7}$$

Equation (6) thus gives the average facet undercooling $-\overline{u}$ as the sum of a capillary term and a kinetic term.

B. Anisotropy function for the surface energy

Optical observations of a pure silicon crystal in contact with its melt showed that both the equilibrium and slow solidification shapes display an alternance of rough and faceted segments [10]. A comparison with phase-field simulations recently allowed to propose an expression of the surface energy anisotropy a_s that was inspired by previous analytical [34, 35] and numerical [23, 24] studies. This anisotropy function has cusps in the $\langle 111 \rangle$ directions and it progressively crosses over to a constant when the interface orientation deviates from these directions. It keeps a constant value for $\alpha \geq \alpha_0$, where α_0 is a parameter that is fixed to 35 degrees here [23]. For $\alpha \leq \alpha_0$, it reads

$$a_s(\alpha) = \frac{\gamma(\alpha)}{\gamma_0} = 1 + \delta|\cos\alpha| + \delta_0|\sin\alpha|, \tag{8}$$

where $\delta_0 = \delta \tan\alpha_0$. As a result, the surface energy $\gamma(\alpha)$ has a cusp at $\alpha = 0$ and it is maximum at $\alpha = \alpha_0$. For $\alpha \geq \alpha_0$, we impose $\gamma(\alpha) = \gamma(\alpha_0)$, which ensures the continuity of both a_s and $da_s/d\alpha$ and prevents the introduction of a spurious cusp at $\alpha = \alpha_0$. For this anisotropy function, BAP equation adopts the more specific form

$$\overline{u} = -2d_0\delta_0/\Lambda - \beta_{111}V_f. \tag{9}$$

III. BASES OF THE PHASE-FIELD MODEL

In order to perform numerical simulations of the physical 2D model described in the previous section, we use a phase-field model [23] that we recently adapted from the original thin-interface model [25, 36]. This model introduced a characteristic length W_0 that represents the width of the interfacial region and a characteristic time τ_0 for the relaxation of the system to a minimum of the free energy. More details about the present phase-field model can be found in the above references. Our implementation makes use of the preconditioned phase field,

$$\psi = \sqrt{2}\tanh^{-1}(\varphi), \tag{10}$$

where φ is the original phase field that varies between $+1$ in the solid phase and -1 in the liquid phase. The preconditioned phase field varies linearly across the solid-liquid interface. It was introduced by Glasner [37] to reduce the simulation times. For the present simulations, we further increase the code efficiency by using Graphics Processing Unit (GPU) parallel programming [38].

A. Phase-field equation

Imposing a frozen temperature field reduces the model to a single evolution equation for the phase field. Taking the interface width W_0, and the relaxation time τ_0 as the length and time units, this equation reads

$$\begin{aligned} a_\tau(\vec{n})\frac{\partial\psi}{\partial t} &= \sqrt{2}\Big[\varphi - a_1\xi(1-\varphi^2)u\Big] \\ &+a_s^2\Big[\nabla^2\psi - \sqrt{2}\varphi(\vec{\nabla}\psi)^2\Big] \\ &+2a_s\vec{\nabla}a_s\cdot\vec{\nabla}\psi \\ &+\frac{\sqrt{2}}{(1-\varphi^2)}\vec{\nabla}\cdot\vec{A}, \end{aligned} \tag{11}$$

where $a_1 \simeq 0.8839$. In function of the scale parameter ξ, the characteristic length and time read $W_0 = \xi d_0$, and $\tau_0 = a_0(d_0^2/D)\xi^3$, D being the Si thermal diffusivity, and $a_0 \simeq 0.5539$ [25]. Following [23] and [29], the anisotropy function a_τ is taken as

$$a_\tau(\vec{n}) = a_s(\vec{n})[a_s(\vec{n}) + a_k(\vec{n})], \tag{12}$$

where

$$a_k(\vec{n}) = b_k(\vec{n})(\beta_{111}/\beta_0), \tag{13}$$

and $\beta_0 \simeq 0.5539 W_0/D$

The three components of the unit vector $\vec{n}$ normal to the solid-liquid interface are calculated along the numerical domain axes x, y, and z. However, the anisotropy function $a_s(n_1, n_2, n_3)$ is expressed in the frame of the three cubic crystal axes [100] [010] [001] that are respectively labelled 1, 2, and 3. Three Euler angles are used to obtain n_1, n_2, n_3 from n_x, n_y, n_z by inverse rotations. Details of the present formulation in terms of the anisotropy vector $\vec{A}$ were recently given in the context of dendritic growth of metallic alloys [39, 40]. The first component of $\vec{A}$ is given by

$$\begin{aligned} A_1 &= \frac{(1-\varphi^2)}{\sqrt{2}}|\vec{\nabla}\psi|a_s\Big[(n_1^2-1)\frac{\partial a_s}{\partial n_1} \\ &+n_1n_2\frac{\partial a_s}{\partial n_2} + n_1n_3\frac{\partial a_s}{\partial n_3}\Big], \end{aligned} \tag{14}$$

components A_2 and A_3 being obtained by circular permutations of the indices $(1, 2, 3)$. The same Euler angles are used to obtain A_x, A_y, A_z from A_1, A_2, A_3 by direct rotations.

Let us remark that our code is written in three dimensions but in this paper we will restrict the calculations to the xz plane as in the reference problem of the previous section. To do this, we use a numerical domain that is two mesh units thick and we impose mirror boundary conditions along y. Then $n_y = 0$ and a_s, a_k and a_τ are functions of the conical angle α solely.

B. Experimental input for the anisotropy functions parameters

1. Free energy

As mentionned above, the anisotropy function $a_s(\alpha)$ of the interfacial free energy given in Eq. (8) has a cusp at $\alpha = 0$. As suggested in [41] the numerical divergences produced by the discontinuity of a_s at the cusp can be avoided by replacing $|\cos\alpha|$ with $\sqrt{\cos^2\alpha + \epsilon^2}$ and $|\sin\alpha|$ with $\sqrt{\sin^2\alpha + \epsilon^2}$. This substitution slightly modifies the values of the anisotropy function, as shown in details in [23] but, except for $\alpha \simeq 0$, the differences are small. In practice, taking a value of $\epsilon^2 = 10^{-4}$ proved satisfactory. The cusp amplitude δ can be obtained by comparing the experimental equilibrium shapes of reference [10] with the ones simulated by our phase-field code. It was noted in [23] that certain shapes shown in [10] are slightly deformed, probably because of a small misalignment of the crystal with the furnace vertical axis. This would explain why the (110) crystal equilibrium shape shown in their original figure (numbered 4f in [10]) does not exactly reproduce the angles expected for the diamond crystal structure. To correct for this misalignment, we first slightly rotate this figure until the angles between two adjacent facets become very close to 110 degrees as expected. We then repeat phase-field simulations of the equilibrium shape for different values of the cusp amplitude δ and compare them with the rotated experimental shape. The best agreement is found for $\delta = 2.5$.

2. Kinetic attachment coefficient

For $\langle 111\rangle$ facets, the kinetic attachment coefficient β_{111} is known to be rather large [17]. The thin-interface phase-field model does allow quantitative simulations of solidification for materials with strong kinetic coefficients. However this model is primarily restricted to linear kinetic undercoolings of the form βV_f. Introducing nonlinear kinetics in a phase-field code is in principle possible but such attempts have resulted in a much higher level of approximation so far [43]. In order to obtain an estimate of β_{111}, the experimental data given in [17] need to be replotted in function of the local undercooling and fitted to a linear curve. Doing so, one obtains the estimate $\beta_{111} \simeq 24.7 \times 10^{-6}$ s/μm.

In the phase-field code one also needs to avoid the strong singularity of $\beta(\alpha)$ resulting from Eq. (2) because the sharp discontinuity of $b_k(\alpha)$ at $\alpha = 0$ causes numerical divergences in practice. The discontinuity is thus replaced in our code by a smooth variation that has the form of a narrow Gaussian,

$$a_k(\alpha) = b_0 \exp\Big[-\Big(\frac{\alpha}{\Delta\alpha}\Big)^2\Big]. \qquad (15)$$

In this expression, α represents the conical angle defined previously, and $\Delta\alpha$ its dispersion. As detailed in the next section, the Gaussian amplitude b_0 is taken proportional to the ratio β_{111}/β_0 in the code.

C. Implementation

1. Initial and boundary conditions

The initial condition is a flat interface located at the isotherm $T = T_m$. Accordingly, the phase field is initially set to $\psi(z) = (z_m - z)/W_0$.

In order to reproduce 2D systems, we reduce the domain size to two mesh points and impose mirror boundary conditions in the y direction. On the left domain side ($x = 0$), the Herring equation must be satisfied by an appropriate boundary condition. Phase-field models that coherently implements triple junction equations have been described in [42]. In the present code, we adopt the less accurate but simpler wetting condition already used in [44],

$$\Big(\frac{\partial\psi}{\partial x}\Big)_{x=0} = \sigma_0(1-\varphi^2), \qquad (16)$$

where σ_0 is a positive constant. This boundary condition only modifies the phase field in the vicinity of the triple point, where the solid-liquid interface contacts the domain boundary. Far from this point, one has $\varphi^2 \simeq 1$, so Eq (16) reduces to a mirror boundary condition. In our simulations the wetting boundary condition (16) causes the liquid phase to partially wet the lateral domain boundary on a thickness of the order of the capillary length d_0. Just beyond this thin liquid film, the solid-liquid interface is almost a straight line with a slope that is exactly the expected crystallographic angle θ_f, as observed in the experiments [45]. We checked that σ_0 can be varied in a rather large domain without affecting the simulated interface shape. For the present purpose, it is thus unnecessary to determine a precise value of this parameter. In order to reduce the computing time, one generally simulates only a half of the domain width, so a mirror boundary condition is imposed on the right domain side located at $x = L$. In addition, we pull back the phase field along the z direction as needed to keep the solidification front at a roughly constant altitude in the numerical domain.

2. Facet length

Rounding the singularities of the interfacial free energy and of the kinetic coefficient as discussed in the previous section somehow changes the nature of the problem. In the 2D reference model, singularities are present and straight ideal facets exist. In the phase-field model, the interface is never quite straight, although the anisotropy functions strongly vary in the vicinity of $\alpha = 0$. Ideal

facets are now replaced with slightly rounded pseudo-facets for which locating the point where the facet contacts the rough segment of the interface depends on a prescribed criterion. To locate the facet end point, we follow the interface points, starting from the facet bottom. Using Eq. (15), we compute the value of the conical angle α (see Fig. 1a) for each of the interface points and we use linear interpolation to find precisely where this angle starts to exceed the prescribed limit $\alpha_{\max}$. In practice, we take $\alpha_{\max} = c_\alpha \Delta\alpha$, so our criterion depends on the specific values chosen for c_α and $\Delta\alpha$.

3. Kinetic coefficient amplitude

In the thin-interface phase-field model, the Gibbs-Thompson equation is necessarily valid at every interface point [25]. However, since we want to compare our simulations results with the reference 2D model for which an ideal facet exists, it is preferable to adjust the amplitude b_0 of the kinetic coefficient used in the phase-field simulations to conform more accurately to the BAP interface equation (9). The first step is to compare the capillary term to the kinetic one on the r. h. s. of this equation. As we will see in the next section, for a facet velocity of the order of $V_f = 10$ μm/s, the facet length is of the order of $\Lambda = 1000$ μm. As a result, the capillary term $\simeq -7 \times 10^{-7}$, while the kinetic term $\simeq -2.5 \times 10^{-4}$. In first approximation, one can thus neglect the capillary term for the pulling velocities used in the simulations, so

$$\overline{u} \simeq -\beta_{111} V_f. \tag{17}$$

In the phase-field simulations, both u and β vary linearly along the pseudo-facet, their ratio being everywhere equal to the facet velocity V_f. We must thus replace the previous equation with the following integral equation,

$$\Lambda \overline{u} = -V_f \int_{s-}^{s+} \beta ds = -\bar{\beta} V_f \Lambda. \tag{18}$$

Integrating from the lowest to the highest facet end, that is from $\alpha = 0$ to $\alpha = c_\alpha \Delta\alpha$, and using Eq. (15) one finally obtains

$$\bar{\beta} = b_0 \beta_0 = \frac{2\beta_{111}}{1 + \mathrm{e}^{-c_\alpha^2}}. \tag{19}$$

In the present simulations, we use $c_\alpha = \sqrt{2}$ but other values are equally valid. For this choice, we must impose $\bar{\beta} \simeq 43.5 \times 10^{-6}$ s/μm for the kinetic coefficient taken in the simulations.

4. Summary of the physical and numerical parameters

We already encountered a number of physical and numerical parameters. These need to be completed by a few ones that are also used in the phase-field code. The value or the range of values taken by each parameter is gathered in Table I. We should emphasize that, as compared to our previous publication on Si solidification, several parameters have been updated here.

Physical parameter	Symbol	Value
capillary length	d_0	1.94×10^{-4} μm
thermal diffusivity	D	2.3×10^7 μm^2/s
specific heat at constant pressure	c_p	1.032 J/g/K
specific latent heat	l_H	1650 J/g
temperature gradient	G	1.08×10^{-3} K/μm
pulling velocity	V	$(2.0 - 22.0)$ μm/s
kinetic coefficient	β_{111}	24.7×10^{-6} s/μm
facet angle for [001]	$\cos\theta_f$	$\sqrt{2/3}$
facet angle for [011]	$\cos\theta_f$	$\sqrt{1/3}$

Numerical parameter	Expression	Value
scale parameter	W_0/d_0	$(0.4 - 2.0) \times 10^4$
grid spacing	h	1.0
cusp amplitude	δ	2.5
cusp rounding parameter	ϵ	0.01
anisotropy domain	α_0	35°
angular dispersion	$\Delta\alpha$	2.3°
facet end criterion	c_α	$\sqrt{2}$
mean kinetic coefficient	$\bar{\beta}/\beta_{111}$	1.762
Euler angles for [001]	$\psi_E, \theta_E, \varphi_E$	$\pi/4, 0, 0$
Euler angles for [011]	$\psi_E, \theta_E, \varphi_E$	$0, \pi/4, 0$

TABLE I: Values of the physical and numerical parameters used in the phase-field simulations.

IV. RESULTS OF THE PHASE-FIELD SIMULATIONS

A. Interface shape

Fig. 3 shows the interface shapes obtained for simulations performed at different pulling velocities V. All these results are obtained for the same value of the scale parameter, $\xi = W_0/d_0 = 5000$, that is for a reasonably small interface width $W_0 = 0.97$ μm. As expected, the increase of the kinetic term βV_f results in the increase of the facet length Λ. Regarding the numerical effort required, we observed that a rather long physical time, up to 450 s, is necessary for the facet length to reach a steady state value at large pulling velocities. This corresponds here to roughly 2×10^7 time steps. In addition, to accommodate larger facets, the domain size, $N_x \times N_z$ mesh points, must be increased with V_f. For the [001] crystal

orientation, the domain is enlarged from 800×1200 to 2000×2400 mesh points (776×1164 to 1940×2328 μm^2) for $V \geq 20.0$ μm/s, and for the [011] direction, from 1000×1200 to 2400×2400 (970×1164 to 2328×2328 μm^2) for $V \geq 12.0$ μm/s. Altogether, the larger systems necessitate about 10 days of running time with a single GPU Nvidia GeForce GTX 1080. Let us recall that the system is 2D here (two mesh points in the thickness). At the moment, 3D simulations of a comparable accuracy are thus out of reach this way.

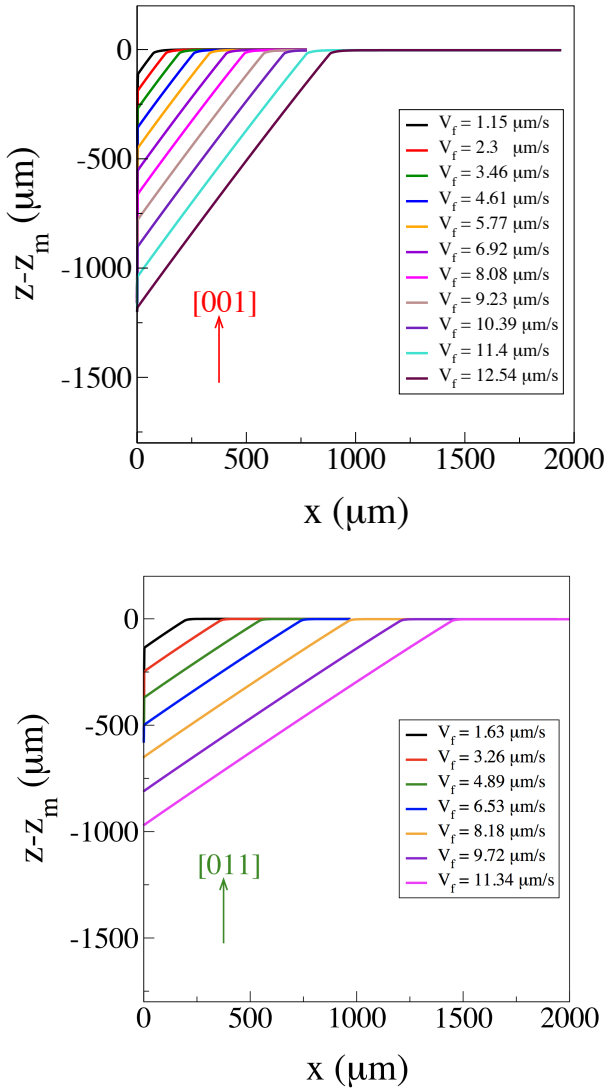

FIG. 3: Interface shapes obtained by phase-field simulations at different pulling velocities for the two crystal orientations [001] and [011]. Values of the facet normal velocity $V_f = V \sin\theta_f$ are indicated.

B. Dependence of the facet length Λ on the angular dispersion $\Delta\alpha$

As discussed in sections III C 2 and III C 3, a criterion is applied to accurately determine the length Λ of the pseudo-facet. Fig. 4a shows the interface shapes obtained for different values of the angular dispersion $\Delta\alpha$ used to smooth out the kinetic coefficient by using a Gaussian anisotropy function a_k (Eq. (15)) instead of a discontinuous one (Eq. (2)). The obtained results show that only a limited range, $\Delta\alpha \in [0.02, 0.06]$, is acceptable in practice. Using larger values of $\Delta\alpha$ causes the code to diverge because then the whole interface adopts a slow growth kinetics. Alternatively, using smaller values causes the facet to disappear because $\Delta\alpha$ then falls beyond the numerical error due to the discretization of α (of order h^2 with $h = 1$ here). To determine the right pseudo-facet end, one compares the local interface conical angle α with $\alpha_{\max} = \sqrt{2}\Delta\alpha$. Fig. 4b illustrates this criterion for the different values of $\Delta\alpha$. The wetting condition imposed on the left domain side (see section III C 1) is necessary to obtain the corresponding facet. It should somehow influence the location of the facet left end. As discussed previously, a very narrow (about 2 μm) liquid groove is created near the domain boundary (see Fig. 4a) and just beyond it the facet conical angle $\alpha = 0$ with a very good accuracy (Fig. 4b). In practice, we thus ignored the groove part and extended the facet down to the left domain boundary. This introduced only minute errors on the measure of Λ. In the following, we use the average value $\Delta\alpha = 0.04$ of the acceptable range found in this study.

C. Convergence with interface thickness

The next necessary step is to test the convergence of these shapes, especially that of Λ, with ξ. The strong variations of the anisotropy function a_τ along the interface suggest that the convergence should strongly depend on the facet normal velocity $V_f = V \cos\theta_f$. To see that, one considers both the facet motion and the phase field diffusion in the direction normal to the facet. In both cases, one can define a characteristic time for the whole interface, that is for a distance $d_I = NW_0$ (we will take $N = 10$ in the following). The physical time necessary for the facet to translate by d_I is simply $t_f = d_I/V_f$, that is

$$t_f = N\frac{d_0}{V_f}\xi. \tag{20}$$

To obtain the diffusion time, one first reduces the phase field evolution equation to its part relative to the phase field diffusion. The result of this operation appears more clearly if one rewrites the evolution equation in terms of the usual phase-field variable φ. One gets then

$$\frac{\partial\varphi}{\partial t} \simeq (a_s^2/a_\tau)\nabla^2\varphi. \tag{21}$$

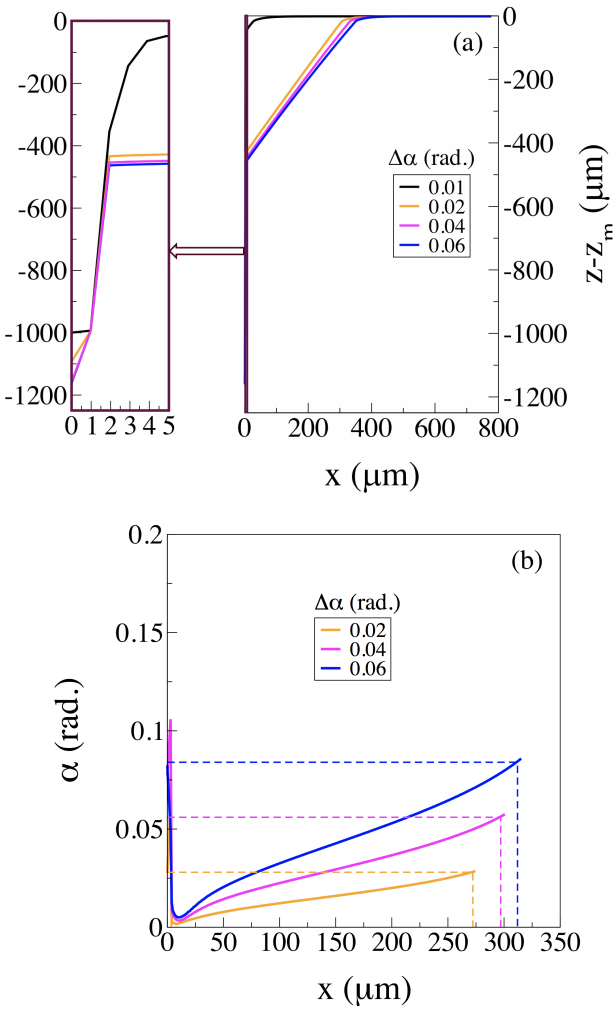

FIG. 4: Influence of the angular dispersion $\Delta\alpha$ on the estimated facet length Λ: crystal orientation [001] and facet growth velocity $V_f = 5.7$ μm/s. (a) Interface shapes showing a pseudo-facet (except for $\Delta\alpha = 0.01$) and horizontal blowup near $x = 0$ of the liquid groove due to the applied wetting condition. (b) Conical angle α calculated along the solid-liquid interface as a function of the spacial coordinate x. The horizontal dashed lines correspond to the criterion $\alpha = \sqrt{2}\Delta\alpha$. The vertical dashed lines indicate the x coordinates of the facet right ends.

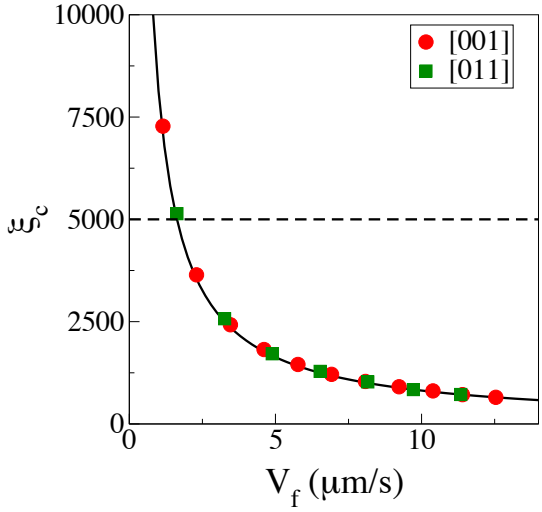

FIG. 5: Convercence scale parameter ξ_c as a function of the facet normal velocity V_f for the two crystal orientations [001] and [011]. For a given V_f, converged results are expected for ξ values below the curve.

The physical time necessary for the diffusion of φ over a distance d_I is thus given by $t_d = N^2 \frac{a_\tau(0)}{a_s^2(0)} \tau_0$. Using the previous expressions of $a_s(0)$, $a_k(0)$, and τ_0, one finally obtains

$$t_d = N^2 \Big[\frac{a_0 \xi^3 d_0^2}{D} + \frac{\bar{\beta} d_0 \xi^2}{a_s(0)} \Big]. \qquad (22)$$

For a given value of the scale parameter ξ, increasing the pulling velocity (thus the facet velocity V_f), will decrease t_f until it becomes smaller than t_d. In this high velocity regime, the diffusion of φ is too slow as compared to the facet translation. The phase field profile can no longer keep a stationary shape in the whole interface so the phase-field simulations start to depart from the physical problem. This can be cured by reducing t_d, thus ξ but the simulations become much longer then (proportionally to ξ^{-5}). In our previous simulations of silicon free growth, we did not encounter this problem because the undercooling was kept very low, so taking $\xi = 10^4$ was sufficient to obtain well-converged results [23]. Conversely, a phase-field study of Ni dendritic growth at large undercoolings and with large kinetic effects showed similar effects as the ones mentioned here, as special efforts proved necessary to simulate heat diffusion accurately at large growth velocities [46].

A convergence scale parameter $\xi = \xi_c$ can be defined by the equality of the two times, $t_d = t_f$. This equality gives a second order equation in ξ_c that is solved analytically. Fig. 5 shows the evolution of ξ_c with the facet velocity V_f. This figure predicts that for simulations performed at $\xi = 5000$, fully converged simulation results are only obtained for the lowest pulling velocity considered here, $V = 2.0$ μm/s, for which $\xi_c > 5000$. This analysis suggests that convergence of the facet length Λ with ξ should strongly depend on the facet velocity; as shown in Fig. 6a,b,c, this is indeed the case. When V_f increases, the convergence curves shift to lower ξ values because ξ_c decreases and to higher Λ values because the kinetic effects increase. It is thus possible to rescale these curves simply by plotting Λ/Λ_0 versus ξ/ξ_c, where both Λ_0 and ξ_c depend on V_f.

In the present analysis, the values for $\Lambda_0(V_f)$ cannot be predicted. In practice, we choose them to ensure a good vertical overlap between the rescaled curves obtained at different velocities V_f. As shown in Fig. 6d, one does obtain a master curve by fitting the rescaled data points obtained at different velocities. This master curve can be

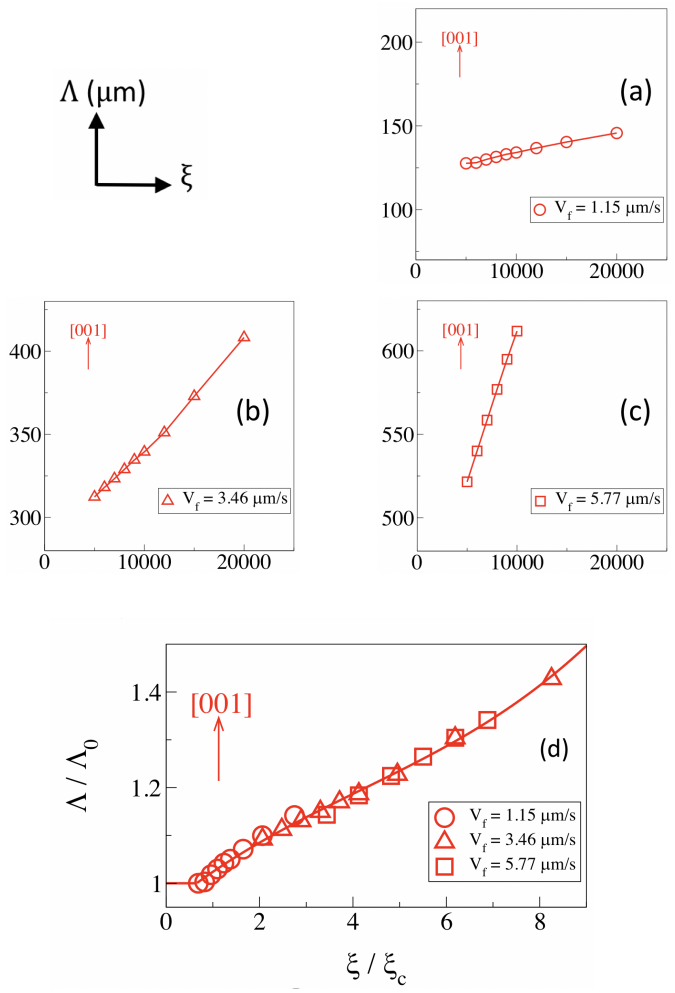

FIG. 6: Convergence of the facet length Λ when the scale parameter ξ tends to zero. Convergence curves for (a) $V_f = 1.15$ μm/s, (b) $V_f = 3.46$ μm/s, and (c) $V_f = 5.77$ μm/s. (d) Master curve merging the three previous series of data (marked by different symbols): the continuous line is a polynomial fit to the whole set of data.

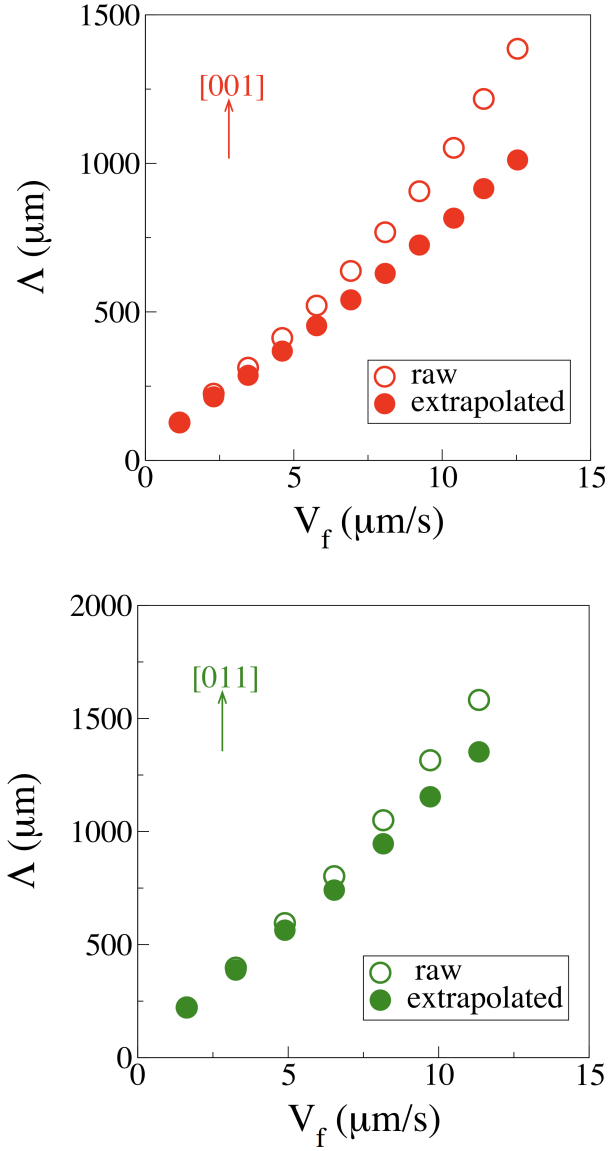

FIG. 7: Facet lengths obtained by phase-field simulations as functions of the facet normal velocity V_f for the two crystal orientations [001] and [011]. Open symbols represent raw data from simulations at $\xi = 5000$. Filled symbols are the values extrapolated from the raw data by using the master curve obtained for the corresponding crystal orientation (see Fig. 6d).

used to extract Λ_0, the value expected for the facet length in the physical limit of vanishing interface width ($\xi \to 0$). Knowing Λ for a simulation performed at a given velocity V_f, one obtains the abscissa $\xi/\xi_c(V_f)$. At this abscissa, the master curve gives an ordinate $\Lambda/\Lambda_0(V_f)$, from which one gets $\Lambda_0(V_f)$. This procedure is used to obtain converged estimates of the facet length in the whole range of velocities explored. The same procedure was followed for the [011] crystal direction for which we obtained a very similar behavior. As shown by the previous analysis, when the facet velocity increases, the phase-field results obtained for a given scale parameter ($\xi = 5000$ here) are expected to depart more and more from those of the asymptotic physical model. Our simulation results confirm this expectation, as one can see in Fig. 7 that the facet length Λ obtained for $\xi = 5000$ increases faster than the converged value Λ_0. For the [001] orientation this deviation is systematically larger than for the [011] one.

V. COMPARISON WITH ANALYTICAL INTERFACE SHAPES

In the present section, we aim at an analytical description of the growth shapes in the reference model. To start with, we introduce the length $z_0 = \frac{l_H}{c_p G}$ that connects the nondimensional temperature field u with altitude z. Then, we form a characteristic length $\ell_0 = \sqrt{d_0 z_0}$. Fi-

nally, for the interface points (x_i, z_i), we introduce their nondimensional coordinates

$$\chi = \frac{x_i}{\ell_0} \quad ; \quad \eta = \frac{z_i - z_m}{\ell_0}. \tag{23}$$

The ideal facet being a straight line, we only consider the function $\eta(\chi)$ that gives the shape of the rough interface segment. For this segment, one can write the field $u_i(\chi)$ in two ways. Using the frozen temperature gradient,

$$u_i(\chi) = \frac{z_i - z_m}{z_0} = \frac{\ell_0}{z_0}\eta(\chi), \tag{24}$$

and using the Gibbs-Thomson equation,

$$u_i(\chi) = -\frac{d_T(\alpha)}{\ell_0}\kappa(\chi) = \frac{d_T(\alpha)}{\ell_0}\frac{\eta''}{(1+\eta'^2)^{\frac{3}{2}}}, \tag{25}$$

where $\eta' = d\eta/d\chi$ and $\eta'' = d^2\eta/d\chi^2$. Combining both expressions, one obtains the differential equation that gives the rough interface shape,

$$[a_s(\alpha) + d^2a_s(\alpha)/d\alpha^2]\eta'' = \eta(1+\eta'^2)^{\frac{3}{2}}. \tag{26}$$

This equation can be solved by a finite-difference integration algorithm. The starting point is the apex of the interface, located on the rightmost point of the domain for which $\chi_L = L/\ell_0$. The interface altitude at this point, $\eta_L = \eta(\chi_L)$ is the input of the calculation. Due to the small positive curvature at this point, η_L must be slightly negative. In addition, the derivative is zero at this point, $\eta'(\chi_L) = 0$.

Integration propagates from this initial point by decreasing χ by a very small amount h_χ (typically $h_\chi = 10^{-4}$) and using series expansions of η and η' as functions of h_χ. The procedure is repeated until η' reaches the value expected for the facet, i. e., $\eta' = \cot\theta_f$. This condition allows to locate the coordinates (χ_F, η_F) of the contact point F with the facet. The facet is a straight line of slope $\cot\theta_f$ starting at $\chi = 0$ and ending at $\chi = \chi_F$. Its length is thus

$$\Lambda = (\chi_F/\sin\theta_f)\ell_0. \tag{27}$$

The vertical distance from point F to the isotherm $T = T_m$ is

$$H = -\eta_F\ell_0. \tag{28}$$

Since the temperature field u varies linearly with z, its average value along the facet is obtained at the facet mid point,

$$\bar{u} = -\frac{1}{z_0}\left(\frac{\Lambda\cos\theta_f}{2} + H\right). \tag{29}$$

Connexion with the growth velocity is now made through the BAP equation (9) from which one gets

$$\beta_{111}V_f = \frac{1}{z_0}\left(\frac{\Lambda\cos\theta_f}{2} + H\right) - \frac{2\delta_0 d_0}{\Lambda}. \tag{30}$$

This second order equation in Λ can be solved analytically, provided the distance H from point F to the isotherm $T = T_m$ is known. To estimate H, we solve numerically the differential equation Eq. (26) that gives the interface shape. Typical values of the two characteristic lengths are $\ell_0 = 16.94$ μm and $z_0 = 1.48 \times 10^6$ μm. Numerical integrations of Eq. (26) are done in a system of width $L \simeq 1940$ μm, for different values of $\eta_L = -1.0 \times 10^{-m}$. For the [001] crystal orientation, we impose $m = 16, 17, 18, \ldots, 25$ and $m = 10, 12, 14, \ldots, 24$ for [011]. For each m value, the facet highest point F is

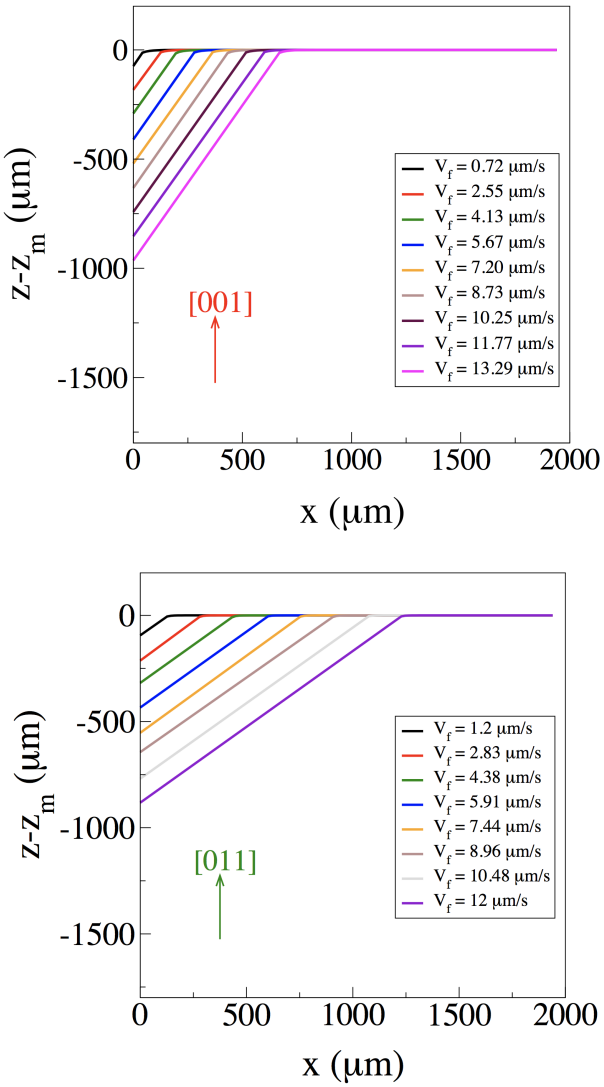

FIG. 8: Analytical interface shapes given by numerical solutions of Eq. (26) for different values of η_L. Crystal orientations [001] and [011].

located. Its distance H to the $T = T_m$ isotherm is found to be almost independent of η_L and we obtain $H \simeq 18.63$ μm for the [001] crystal orientation ($H \simeq 10.27$ μm for [011]).

The corresponding numerical solutions of Eq. (26) are

represented in Fig. 8 for the two crystal orientations considered. Knowing H and Λ, the facet growth velocity V_f can be obtained from Eq. (30). The η_L values have been chosen to roughly obtain V_f values comparable to the ones used in the phase-field simulations (see Fig. 3).

Alternatively, equation (30) is solved to obtain Λ, from the knowledge of H and for arbitrary values of V_f. The resulting curves for the [001] and [011] crystal orientations are displayed in Fig. 9, together with the Λ_0 values obtained by extrapolating the Λ phase-field data to $\xi = 0$. The agreement is very satisfactory, deviations of less than 10 percent being systematically found. This gives good confidence that quantitative simulations can be performed with our phase-field model, provided that care is taken to adjust the numerical parameters to the experimental ones and also to extrapolate the simulation data to the limit of vanishing interface thickness.

VI. SUMMARY AND DISCUSSION

In summary, we carried out a study that assessed the potential of the phase-field model to tackle quantitatively directional solidification of materials exhibiting faceted solid-liquid interfaces. This was made possible by defining a simple but realistic analytical model that describes the directional solidification of a monograin and by solving this analytical model. Simultaneously, we performed phase-field simulations for the same physical problem. Finally, comparing the simulation results to the analytical ones confirmed the phase-field model quantitativeness.

Regarding the link with a real material (silicon here), we updated the anisotropy functions both for the surface energy and the kinetic attachment coefficient by reanalyzing recent experimental data of the literature. The analytical expressions of the anisotropy functions were directly taken from our previous study [23], where they were validated by comparisons with experimental images for the equilibrium and the slow growth of a single Si grain [10].

We introduced a simple 2D reference model that follows the crystal orientations of real thin samples presenting a high degree of invariance in the direction perpendicular to the sample plane [17]. The temperature field was assumed frozen, a choice that was well justified for the moderate solidification velocities concerned. For this model, the shape of the rough segment of the solid-liquid interface was shown to be given by a exact differential equation for which we found numerical solutions.

In parallel, we introduced a phase-field equation to simulate the evolution of the solid-liquid interface in the 2D reference model. We found it particularly important to control two independent steps in order to reach a good level of accuracy in the simulations. The first step was to tune the amplitude of the kinetic term to the criterion chosen to measure the facet lengths. The second step was to obtain a master curve that allows to extrapolate facet lengths to the limit of zero interface width.

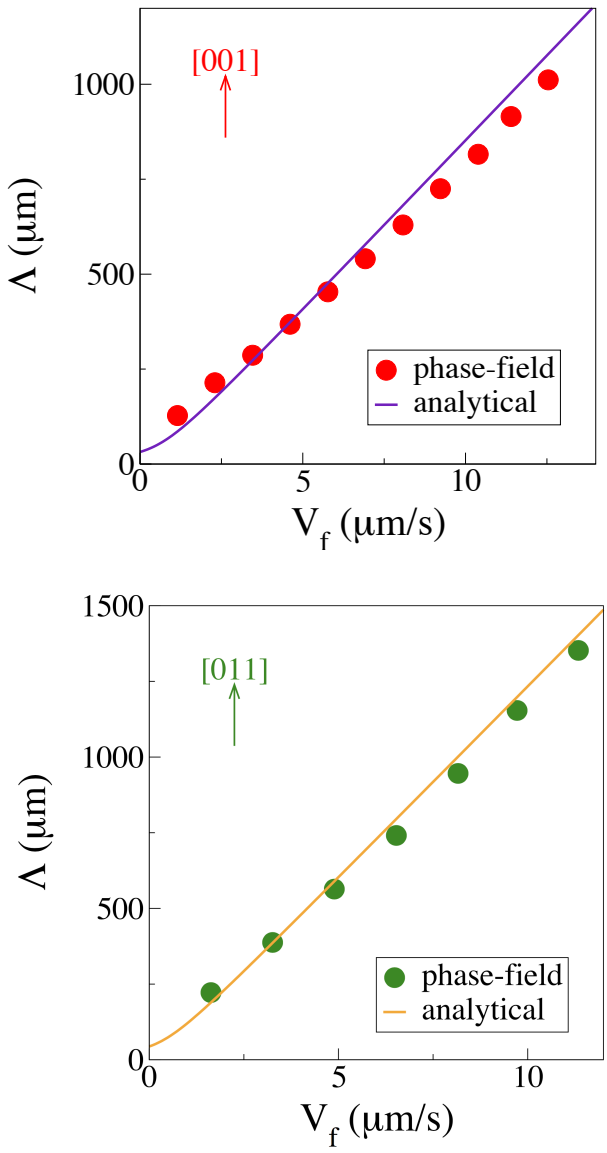

FIG. 9: Facet length as functions of facet velocity for the two crystal orientations [001] and [011]. Symbols are the extrapolated facet lengths predicted by the phase-field simulations. Lines are deduced from the analytical model.

Both steps being performed, we were able to compare the results obtained by solving the analytical model to the ones obtained by phase-field simulations. Direct comparisons were made for two crystal orientations, [001] and [011]. In both cases, the analytical and the simulation results agreed over the whole range of pulling velocities, with accuracy of a few (less than ten) percent.

Albeit for its simplicity, the present reference model is rather close to real experimental situations. We can thus expect that comparable phase-field simulations can be performed in various situations where additional features are required to account for experimental specificities.

One can think for instance of thickness effects, nontrivial crystallographic orientations, grain boundaries, and so on. In addition, it would also be desirable to determine the evolution of the temperature field if one wants to predict the system behavior at higher pulling velocities for instance.

Acknowledgments: Part of this work was funded by the ANR project CrySaLID (N°ANR-14-CE05-0046-01). We thank Nathalie Mangelinck-Noël and Guillaume Reinhart for very useful discussions and for providing the experimental picture shown in Fig. 1b. We also thank Kozo Fujiwara for interesting discussions on different aspects of silicon solidification, notably about one experimental setup used in his group.

[1] *Third Generation Photovoltaics* (Springer 2003), Martin A. Green.
[2] *Solar Cells: Materials, Manufacture and Operation* (Elsevier, 2013), A. McEvoy, T. Markvart, L. Castañer eds.
[3] *Crystal Growth of Si Ingots for Solar Cells using Cast Furnaces* (Elsevier, 2020), Kazuo Nakajima.
[4] G. S. May and C. J. Spanos, *Fundamentals of Semiconductor Manufacturing and Process Control* (Wiley-Intersciences, 2006), chap. 1.
[5] S. A. McHugo, A. C. Thompson, I. Périchaud, and S. Martinuzzi, Appl. Phys. Lett. **72**, 3482 (1998).
[6] G. Stokkan, Y. Hu, Ø. Mjøs, M. Juel, Sol. Energy Mater Sol. Cells **130**, 679 (2014).
[7] G. W. Alam, *Influence of seeding and growth conditions on grain selection, defects, and properties of High-Performance Multicrystalline Silicon (HPmc-Si)* Ph. D. Thesis, Aix-Marseille Université (2017).
[8] K. A. Jackson in *Liquids Metals and Solidification* (ASM, Cleveland, Ohio 2003), p. 174.
[9] U. Landman, W. D. Luedtke, R. N. Barnett, C. L. Cleveland, M. W. Ribarsky, Emil Arnold, S. Ramesh, H. Baumgart, A. Martinez, and B. Khan, Phys. Rev. Lett. **56** 155 (1986).
[10] X. Yang, K. Fujiwara, K. Maeda, J. Nozawa, H. Koizumi, and S. Uda, Progr. in Photovolt. Res. Appl. **22**, 574 (2014).
[11] J. Pohl, M. Műller, A. Seidl, and K. Albea, J. Cryst. Growth **312**, 1411 (2010).
[12] G. Barinovs, A. Sabanskis, and A. Muiznieks, J. Cryst. Growth **391** 13 (2014).
[13] W. Miller and A. Popescu, Acta. Mater., **140**, 1 (2017).
[14] K. Fujiwara, K. Nakajima, T. Ujihara, N. Usami, G. Sazaki, H. Hasegawa, S. Mizoguchi, and K. Nakajima, J. Cryst. Growth **243**, 275 (2002).
[15] T. Duffar, *Recent Research Developments in Crystal Growth, Vol. 5* (2010) p. 61.
[16] M. Trempa, C. Reimann, J. Friedrich, G. Műller, and D. Oriwol, J. Cryst. Growth **351**, 131 (2012).
[17] V. Stamelou, M. G. Tsoutsouva, T. Riberi-Bridot, G. Reinhart, G. Regula, J. Baruchel, and N. Mangelinck-Noël, J. Cryst. Growth **479**, 1 (2017)
[18] J. Eggleston, G. McFadden, and P. Voorhees, Phys. D **150**, 91 2001).
[19] A. Wheeler, Proc. R. Soc. A**462**, 3363 (2006).
[20] B. J. Spencer, Phys. Rev. E **69**, 011603 (2004).
[21] S. Torabi, J. Lowengrub, A. Voigt, and S. Wise, Proc. R. Soc. A**465**, 1337 (2009).
[22] T. Philippe, Phys. Rev. E **103**, 032801 (2021).
[23] A. K. Boukellal, A. K. Sidi Elvalli, and J.-M. Debierre, J. Cryst. Growth **522**, 37 (2019).
[24] J.-M. Debierre, A. Karma, F. Celestini, and R. Guérin, Phys. Rev. E **68** , 041604 (2003).
[25] A. Karma and W. J.Rappel, Phys. Rev. E **57**, 4323 (1998).
[26] A. Karma, Phys. Rev. Lett. **87**, 115701 (2001).
[27] B. Echebarria, R. Folch, A. Karma, and M. Plapp, Phys. Rev. E **70**, 061604 (2004).
[28] H. K. Lin, C. C. Chen, and C. W. Lan, J. Cryst. Growth **362**, 62 (2013).
[29] H. K. Lin, C. C. Chen, and C. W. Lan, J. Cryst. Growth **385**, 134 (2014).
[30] H. K. Lin and C. W. Lan, J. Cryst. Growth **401**, 740 (2014).
[31] P. C. Bollada, P. K. Jimack, and A. M. Mullis, Comput. Mater. Sci. **144**, 76 (2018).
[32] C. Herring, *Surface Tension as a Motivation for Sintering.* In *Fundamental Contributions to the Continuum Theory of Evolving Phase Interfaces in Solids* (Springer, 1999), J. M. Ball, D. Kinderlehrer, P. Podio-Guidugli, and M. Slemrod eds.
[33] M. Ben Amar and Y. Pomeau, Europhys. Lett. **6**, 609 (1988).
[34] M. Adda Bedia and V. Hakim, J. Phys. I France **4**, 383 (1994).
[35] M. Adda Bedia and M. Ben Amar, Phys. Rev. E **51**, 1268 (1995).
[36] A. Karma and W. J. Rappel, Phys. Rev. E **51**, R3017 (1996).
[37] K. Glasner, J. Comput. Phys. **174**, 695 (2001).
[38] *CUDA Fortran for scientists and engineers: best practices for efficient CUDA Fortran programming* (Elsevier 2004), G. Ruetsch and M. Fatica.
[39] A. K. Boukellal, J.-M. Debierre, G. Reinhart, and H. Nguyen Thi, Materialia **1**, 62 (2018).
[40] A. K. Boukellal, M. Rouby, and J.-M. Debierre, Comput. Mater. Sci. **186**,110051 (2021).
[41] N. Wang, M. Upmanyu, and A. Karma, Phys. Rev. Materials **2**, 033402 (2018).
[42] J. A. Warren, T. Pusztai, L. Környei, and L. Gránásy, Phys Rev B **79**, 014204 (2009).
[43] S. H. Liu, C. C. Chen, and C. W. Lan, J. Cryst. Growth **362**, 106 (2013).
[44] J. Ghmadh, J.-M. Debierre, J. Deschamps, M. Georgelin, R. Guérin, and A. Pocheau, Acta Mater. **74**, 255 (2014).
[45] T. Riberi-Bridot, M. G. Tsoutsouva, G. Regula, G. Reinhart, F. Guittonneau, L. Barrallier, and N. Mangelinck-Noël, Acta Mater. **177**, 141 (2019).
[46] J. Bragard A. Karma, Y. H. Lee, and M. Plapp, Interface Science **10**, 121 (2002).